Supplementary information for: **The vertical structure of CO in the Martian atmosphere as observed by ACS on ExoMars TGO**

K. S. Olsen[1,2*], F. Lefèvre[2], F. Montmessin[2], A. A. Fedorova[3], A. Trokhimovskiy[3]
L. Baggio[2], O. Korablev[3], J. Alday[1], C. F. Wilson[1], F. Forget[4], D. A. Belyaev[3],
A. Patrakeev[3], A. V. Grigoriev[3], and A. Shakun[3]
[1] Department of Physics, University of Oxford, Oxford, UK,
[2] Laboratoire Atmosphères, Milieux, Observations Spatiales (LATMOS),
Université Paris-Saclay, Sorbonne Université,
Centre National de la Recherche Scientifique (CNRS),Guyancourt, France,
[3] Space Research Institute of the Russian Academy of Sciences (IKI RAS), Moscow, Russia
[4] Laboratoire de Météorologie Dynamique (LMD), Sorbonne Université, CNRS, Paris, France,

November 11, 2020

This PDF file contains supplementary information for **The vertical structure of CO in the Martian atmosphere as observed by ACS on ExoMars TGO**. The supplementary information contains Supplementary Methods and Supplementary Figures 1–7.

Supplementary Methods

We use data from the mid-infrared channel (MIR) of the Atmospheric Chemistry Suite (ACS) [1] that was collected between April and September 2018 (Ls 164°–220°). Our results feature strong variability with latitude, and higher mixing ratios are observed towards the poles. Some longitudinal variability in CO has been noted (e.g., [2]), but the solar occultation observations are too sparse to probe this at this time.

ACS MIR is a cross dispersion spectrometer consisting of an echelle grating with a wide blaze angle and a secondary, steerable diffraction grating [1]. It has the finest spectral resolution of any atmospheric remote sensing instrument at Mars and operates in solar occultation mode, which provides high signal-to-noise, a long optical path length, and sensitivity to vertical structure (vertical resolution of 1–5 km). The 2-0 band of CO is observed in secondary grating position 7, which has a wavenumber range of 4180–4430 cm^{-1} and spectral resolution of 0.06–0.065 cm^{-1}.

Fig. 1 shows a typical ACS MIR spectrum featuring the 2-0 band of CO. Panel (a) shows normalized transmission spectra from a single occultation at 60 km. The colours and dashed lines indicate that the observed spectral range is divided among eight distinct diffraction orders (250–257). Panel (b) shows an example spectral fit for one order (252) and the associated residuals. The majority of absorption lines shown are from the primary CO isotopologue ($^{12}C^{16}O$), while smaller features at lower wavenumber come from the minor isotopologues of CO ($^{13}C^{16}O$ and $^{12}C^{18}O$). There are no other interfering species in this spectral region.

1 Calibration of ACS MIR transmission spectra

ACS MIR data are processed in several stages. Raw data are sent from the European Space Astronomy Centre (ESAC) to the Russian Space Research Institute (IKI), where a Level 0B data product is created. Detector images contained in the Level 0B data product undergo several corrections including correcting hot pixels and accumulation errors, removing the dark background and flat field, vertical and horizontal sub-pixel registration, subtracting stray light and performing an orthorectification transformation (Levels 1A/B). After that, transmission spectra (Level 2A) are computed using a reference observation of the sun, and the observations made during atmospheric occultation.

There are two distinct groups generating Level 1A and Level 2A data products (detector images of corrected transmission): IKI and LATMOS. The ACS MIR position 7 spectra used in this study were produced at LATMOS. The following sections describe the Level 0B, 1A/B, and 2A data products for ACS MIR.

1.1 Level 0B: raw data description

Level 0B data consist of a collection of 16-bits monochrome images (640×512 pixels). These are the result of on-board averaging of either 200 or 96 individual acquisitions (or *framelets*) of the detector array with 3 ms exposure time. Each image captures a small range of wavenumbers dispersed horizontally by the echelle high resolution diffraction grating. Overlapping diffraction orders are discriminated by a rotating perpendicular secondary grating and they end up separated vertically by about 30 pixels. See [1] for a description of the optical setup, and refer to Supplementary Fig. 1 for an example of a detector frame (Level 1A).

The sun light is collimated using a narrow entrance slit on the focal plane of the telescope, and its image on the detector array covers a vertical extent of about 25 pixels in height, each of them corresponding to a different pointing on the sun disc (obtaining a total field of view of ~ 3 km).

The collection of all wavelengths (x-axis) and pointing directions (y-axis) from one diffraction order forms an horizontal *stripe*, barely fitting within the vertical separation between consecutive diffraction orders (see Supplementary Fig. 1). About 16 of them fit in the detector frame, for the secondary grating position setup used in this study.

1.2 Level 1A/1B: data cleaning and preprocessing

The raw data products are affected by several known issues, belonging to five different categories, that are corrected to a certain extent:

1. Digital signal processing on-board.
    - frame serialization lag : row/column appear our of sync after deserialization of transmitted data; correction consists in a simple reordering, but for the loss of the 6 top-right corner pixels of each frame.
    - one or more individual corrupt framelets within one averaged frame: uncorrectable, whole frame flagged and discarded ($\sim 5\%$ frames lost).
    - individual partial rows ($\sim 10 - 20\%$ per frame) with various kinds of averaging errors: mostly recoverable, but for ~ 1 row every 5 frames flagged as uncorrectable.
2. Electronic/readout artifacts.
    - Hot pixels, cosmic rays damage or other singular defects: $\sim$ 300 pixels per frame flagged as unusable.
    - Unbalanced non-linear response ($\sim 0.1\%$) of the 4-way A/D converter: modelled and mostly compensated for.
    - Pixel-to pixel non uniformity (both in offset and gain, $\sim 2\%$ of the signal): compensated down to the $\sim 0.05\%$ level.

- Anomalous signal offset: an uniform negative constant offset always anti-correlated with the total input power: estimated and subtracted on a frame-by-frame basis.

3. Background light.

   - thermal noise: a strong ($\sim 200\%$ of full sun signal) but rather featureless signal, slightly varying with time ($\sim 0.1\%$ over a session); it is estimated using dark frames measured at the beginning or end of each observation session, and subtracted to all frames.
   - stray light: out-of-optical path solar light that finds its way into the detector ($\sim 5\%$ of full sun signal). It is estimated by fitting a fixed 2D empirical template extracted from the dark regions in the image and normalized in amplitude on a frame by frame basis.

4. Image registration and rectification.

   - vertical registration: the image drifts vertically ($\sim 0.1 - 2$ pixels per session) probably due to a slow change in the tilt of the secondary mirror. The bottom edge of one order stripe is used as a reference to cross-register the frames by interpolation.
   - horizontal registration: slow ($\sim 0.1 - 0.5$ pixels per session) variation in the horizontal (spectral) position, estimated using a few solar lines as a reference, then corrected by interpolation.
   - pointing errors: residual movement of the spacecraft pointing relative to sun disc; estimated at ± 0.3 pixels, it is only loosely compensated by radiometric correction based on the apparent change of luminosity of the sun correlated with sun limb movement in the field of view.
   - orthorectification: the image is interpolated on a nonlinear (curved) reference such that in the new coordinate set all pixels in one row refer to the same field of view.

5. Image doubling: uncorrected, see Section 1.4.

The result of corrections for categories 1 and 2 is an intermediate level 1A data product, while background subtraction and image registration and rectification define the level 1B, which is precursor to level 2 products. Pointing errors and double image are dealt with at level 2.

An example of a raw detector frame after applying the above corrections is shown in Supplementary Fig. 1. The visible stripes correspond to different diffraction orders. Therefore, the x-axis corresponds to wavenumbers, but the wavenumber scale is unique for each stripe. The y-axis width of each stripe corresponds to the vertical field of view of the instrument (~ 3 km), so each pixel row presents a unique spectrum through adjacent and nearby tangent layers.

1.3 Level 2A: transmission spectra

Level 2A data consists of an image of transmittances for each altitude observed in an occultation. The x-axis corresponds to wavenumber, and the y-axis corresponds to diffraction order, similarly to the Level 1 data shown in Supplementary Fig. 1.

A bias factor representing small changes over time in solar pointing is applied to each observation. A solar-reference image is created by averaging eight observations made above the atmosphere. Images of transmission data are then generated by dividing each radiance image by the solar reference.

The first step in processing Level 2A transmission images for spectral fitting is to select rows for analysis. We are currently working with single spectra near the edge of the optical entry slit, which is identified as the inflection point of an incident light intensity curve for a given order, which is a column of an image as shown in Supplementary Fig. 1.

For each diffraction order, an individual transmission spectrum is extracted near the slit edge of the incident optics (closest to the centre of the sun) and a unique wavenumber calibration is determined, starting from a first-guess wavenumber vector. The corresponding row of the solar reference observation (made outside the atmosphere) is used to perform wavenumber calibration by fitting peak positions of solar lines to a reference solar atlas measured by the Atmospheric Chemistry Experiment Fourier Transform Spectrometer

(ACE-FTS) [3]. If strong absorption lines of CO_2, H_2O, or CO are present in an order's spectral range, the wavenumber calibration is refined by comparing measured absorption line centres to modelled spectra of the target gas contributions.

Spectra are normalized before fitting to correct errors in the baseline level and to mitigate curvature in the baseline that results from variations in the intensity and, therefore signal-to-noise, from the spectra centres to their wings (note the horizontal change in brightness in Supplementary Fig. 1). A baseline function is determined by fitting the spectra using local polynomial regression. A filter is applied to remove strong spectral absorption features, which impact the local regression, and the regression technique is applied again to obtain a smooth curve representing the spectral baseline. The spectra are normalized by dividing by this baseline function.

1.4 Instrument line shape and doubled images

Shortly after the start of the nominal science phase, we observed that each absorption line was mapped into a set of twin lines. In fact, the entire 2D image appears to be focused on the detector twice, with a small vertical ($\sim$ 5 pixels) and horizontal ($\sim$ 2 pixels) offset. We determined that this was likely the result of a faulty optical element between the echelle grating and the detector. Ray tracing simulations suggests that a crack in one lens in the collimator before the detector could produce a similar result, and that may have occurred during the launch.

Work is ongoing to fully parameterize the image-doubling, the magnitude of which varies across the detector array, and to try to mitigate it via deconvolution. Currently, we rather choose spectra in such a way as to maximize the ratio of the magnitude of the doubled image.

Supplementary Fig. 2 illustrates the nature of the doubled image by comparing detector images from two sequential grating positions that capture the same diffraction order, but in the top and bottom of the detector frame. When the rotational unit of the secondary diffraction grating is set to position 6, the radiance spectrum for diffraction order 250 happens to be captured in the lower part of the detector array, occupying a horizontal stripe around row 40. This is shown in Supplementary Fig. 2b. In Supplementary Fig. 2c, the same diffraction order is shown captured a couple of seconds later with the secondary grating switched to position 7. In this case the row number is around 420. By comparing the two images we remark that in the latter detector area the image resolution is degraded. From the radiances in panels (b) and (c) we can compute the transmission spectra shown in panels (d) and (e), respectively, where the effect is easier to see. The schematic drawing in panel (a) depicts the interpretation of this phenomenon: the diffraction order stripe is imaged twice (here in red and blue). Because the secondary image is offset horizontally and vertically, this produces a characteristic blur in the stripe edges and an effective doubling of the absorption lines.

Thanks to the vertical offset of the secondary image, by working near the slit edge, we are able to use spectra in which the magnitude of the secondary peaks are less than 15% those of the primary. The total absorption is conserved, so the secondary peak must be accounted for to ensure accurate retrievals. Across each diffraction order, we measure the separation between the primary and secondary peaks, and the relative amplitude of the secondary peak, which is allowed to vary with wavenumber, but constrained to a linear relationship empirically determined for each order in an occultation. These parameters are used to build an instrument line shape (ILS) consisting of two Gaussian features. The full-width at half-maximum (FWHM) of the Gaussian elements is three detector pixel-widths and is therefore wavenumber-dependent.

An example ILS and its contributing elements are shown in Supplementary Fig. 3a. Supplementary Fig. 3b shows all the spectra for one order simultaneously recorded in a detector frame (a stripe in Supplementary Fig. 1). Each spectrum represents a different tangent altitude, with a vertical separation of $\sim$ 100–150 m, and the baseline offsets are due to altitude-dependent changes in aerosol attenuation. The relative amplitudes of the primary spectral features and their doubles can be seen. See Fig. 1 for a representative example of the spectra used in retrievals. The accuracy of retrievals performed on such spectra using this type of ILS has been determined by intercomparison with retrievals from the NIR channel, which simultaneously observes the same air mass using different instrumentation and analysis techniques. This has been done for H_2O [4] and CO (see Section 5).

2 T and P retrievals with ACS NIR

Where available, CO_2 lines across an absorption-rotation band observed by ACS MIR are fit by the GGG retrieval code (see Section 3). Their fitting results relative to one another are evaluated to estimate corrected vertical profiles of T and P [5]. However, in position 7 there are only very weak CO_2 absorption lines, so we use retrieved T and P profiles from simultaneous observations made by the near-infrared (NIR) channel of ACS [6, 4].

The NIR instrument is a cross dispersion spectrometer combining an acousto-optical tunable filter (AOTF) with an echelle grating [1], and deriving heritage from the SPICAM and SPICAV instruments on Mars Express and Venus Express. The NIR instrument makes solar occultation observations simultaneously with the MIR channel. The instrument has a coarser spectral resolution, but observes strong CO_2 features at all times and can make accurate retrievals of T and P from the surface (or dust top) up to 90 km.

The retrieval scheme employed follows that of SPICAM and is generally described in [7, 8, 9], with updates for NIR given in [4]. The NIR instrument uses diffraction order 49 (6318–6387 cm^{-1}) to retrieve density and temperature vertical profiles from CO_2 absorption features. Transmission spectra are computed from the raw NIR data. The wavenumber calibration is corrected using strong gaseous absorption features. A spectrum is computed for each tangent altitude from an assumed temperature and pressure and volume absorption coefficients from HITRAN 2016 [10].

Fitting is done using a Levenberg-Marquardt minimization scheme that adjusts the temperature, pressure, and CO_2 volume mixing ratio (VMR) to achieve a best fit to the temperature-dependent rotation structure of the CO_2 band in order 49. From the initial retrieval results, an altitude level is selected where the uncertainties, taken from the covariance matrix, are minimum. This pressure level is fixed and the retrieved temperature profile is integrated to obtain a corrected pressure profile that is consistent with the hydrostatic law. This process is iterated again with a fixed pressure profile to obtain a corrected temperature profile. Several iterations are made until the temperature and pressure profiles converge.

Temperature and pressure profiles retrieved from the ACS NIR data have been validated using results from the Mars Climate Sounder and ACS MIR [6, 4]. The MIR and NIR results are consistent for temperature, pressure, and H_2O. Comparison with MCS is more complicated, but no biases between the instruments have been identified.

3 VMR retrievals with ACS MIR

Spectral fitting of ACS MIR spectra is done using the JPL Gas Fitting Software Suite (GGG) maintained by NASA's Jet Propulsion Laboratory [e.g., 11, 12]. GFIT, the spectral fitting component of GGG, was derived from early versions of the Occultation Display Spectra (ODS) software developed for the ATMOS spectrometer flown on the space shuttles [13]. The primary users are the MkIV balloon missions [14] and the Total Carbon Column Observing Network (TCCON) [15].

Spectral fitting for a full occultation is divided into a set of detector frames for each observed tangent altitude, then into a set of extracted spectra for each diffraction order, and then further into spectral fitting windows. For each order, three windows 4–6 cm^{-1} wide are used, allowing for variations in the ILS, and covering only the central part of the spectrum, where the signal-to-noise ratio (SNR) is highest. Fitting is done using a non-linear Levenberg-Marquardt least squares method to compare the measured spectrum to a computed spectrum. The computed spectrum is calculated line-by-line from pre-computed volume absorption coefficients for each gas in a chosen spectral range. We use the 2016 edition of the HITRAN spectroscopic database [10, 16] with additional parameters for line broadening in a CO_2-rich atmosphere where available [e.g., 17, 18, 19]. *A priori* vertical profiles of temperature and pressure are retrieved from simultaneous observations made by ACS NIR.

The state vector contains the continuum level and tilt, a small wavenumber shift, and the VMR scaling factors (VSFs) for each target gas. GFIT is capable of fitting multiple gases at the same time. Minor interfering species in the fitting windows are H_2O, and CO_2 (below 4215 cm^{-1}). Due to differences in arean and terrestrial isotopic ratios, the isotopologues of CO are fitted independently. The first isotopologue

($^{12}C^{16}O$) is dominant in this region, and a band of the third isotopologue ($^{12}C^{18}O$) is overlapping at lower wavenumbers.

The VSF is a multiplicative scaling factor applied to the *a priori* VMR vertical profile. In principle, GFIT only modifies the magnitude, and not the shape of, the *a priori* VMR vertical profile. However, in solar occultation mode, the *a priori* can be scaled for each observed spectrum at each tangent altitude. To retrieve VMR vertical profiles for a target gas from a set of solar occultation spectra, the set of retrieved slant columns abundances from each observation are inverted with the matrix of calculated slant column paths traced through the atmosphere using a linear equation solver. This inversion is also performed using a Levenberg-Marquardt routine and the uncertainties of target gas VMR at each altitude are computed from the Jacobian matrix of partial derivatives.

While all aspects of the data processing and retrieval scheme impact the results, we have found that three factors are critical for CO retrievals with ACS MIR: background light subtraction, *a priori* temperature and pressure, and ILS. The background light subtraction is part of the Level 1A to 2A processing. Its importance was identified while investigating water vapour with ACS MIR and NIR. The practical impact of this correction is to adjust the baseline level while preserving line depth. Without making this correction, retrievals with ACS MIR data underestimate VMRs when compared with ACS NIR or the LMD general circulation model (GCM). The CO VMR is strongly dependant on the density of the atmosphere, which is computed from the temperature and pressure. Changes to the *a priori* temperature and pressure result in very large differences in retrieves CO VMR. We are relying on retrieved temperature and pressure data when possible. The impact of temperature and pressure, and a preliminary comparison with ACS NIR are given in the following sections. Finally, if the ILS is poorly parameterized, and the double image is not accounted for, retrievals with ACS MIR data can strongly underestimate target gas VMRs, as a significant portion of absorbed light is ignored.

4 Modelling of CO with the LMD-GCM

We initially use output from the LMD Mars Climate Database (version 5.3) [20, 21] to provide *a priori* vertical profiles of temperature, pressure, and of CO VMR for comparison. However, the time period covered by our observations was punctuated by a global dust storm, which results in strong heating of the atmosphere, and expansion of the lower layers, and elevation of the water vapour hygropause. Retrievals of temperature and pressure from ACS MIR (using different secondary diffraction grating positions that provide access to CO_2 vibration-rotation bands) and ACS NIR quickly showed a strong departure from the standard climatological scenarios, which do not account for the size of the observed dust storm, nor the magnitude of dust lofted.

A new climatology of dust opacities for Mars year 34 has been reconstructed from Mars Climate Sounder observations [22]. The LMD GCM has been run using this dust climatology in order to better estimate the physical state of the Martian atmosphere, and the impact that has on the abundances of water vapour and CO. Temperature profiles obtained this way tend to be much warmer than those from the MCD, and compare closer to those retrieved.

Vertical profiles of temperature obtained this way are shown in Supplementary Figs. 4a and c, where the two panels distinguish whether the profiles were obtained before or after the onset of the global dust storm. These panels also compare these profiles with retrievals from ACS NIR (solid colours). The difference between the ACS NIR and GCM temperatures is shown in Supplementary Figs. 4b and d. Before the dust storm, we see a bias between the two data sets where the NIR temperatures are 5-10 K warmer than those predicted by the GCM. After the onset of the dust storm, the GCM predicts warmer temperatures than observed by ACS NIR, with a large variability in the differences, but on the order of 10 K. we find that the shape of the temperature profiles is consistent between below 60 km (difference profiles are straighter)

The differences observed between these two temperature data sets (and the MCD as well) have a strong impact on ACS MIR CO VMR vertical profile retrievals. Secondary grating position 7 results in a spectral range that does not provide access to a CO_2 band suitable for temperature and pressure retrievals so an external source must be used.

An example of the impact that each temperature and pressure model has on ACS MIR retrievals is shown

in Supplementary Fig. 5. The example shown is an occultation observed shortly after the dust storm began on Ls 197° and at mid-northern latitude (49°). Supplementary Fig. 5a shows VMR vertical profiles of CO obtained from the MCD and GCM, and retrievals using ACS MIR data and temperature and pressure models provided by the MCD, the GCM, and ACS NIR. It also shows a preliminary CO VMR data product retrieved from the ACS NIR data. A comparison of CO VMR vertical profiles retrieved from coincident ACS NIR and ACS MIR spectra is given in Section 5. In this example, we see a strong deviation in the lower altitude temperatures between the ACS NIR retrieval (purple) and the original predicted temperatures from the MCD (green) (recall Supplementary Fig. 4e). After ingesting the MY 34 dust climatology, the temperatures predicted by the GCM are much closer to the ACS NIR temperature retrieval, though they are still warmer below 60 km and cooler than ACS NIR above. The pressure profiles are shown in Supplementary Fig. 4b and the MCD pressures are greater than those from the GCM and ACS NIR retrieval.

Between 25–65 km, the CO VMRs retrieved from ACS MIR and NIR data are in close agreement. Above 70 km, the CO lines observed by ACS NIR become too weak for accurate spectral fitting (they also overlap a stronger CO_2 band). Both retrievals result in much larger CO VMRs than predicted by the GCM. This is likely a result of the difference between the predicted and observed physical state of the atmosphere (temperature, pressure, and density). When we perform the retrieval using ACS MIR data, and the temperature and pressure predicted by the GCM (green), which is warmer than the ACS NIR observation below 60 km, we find that the resulting VMR is lower by 5–10%. When we use the MCD temperature, which is much warmer, and pressure, which is higher, we find a further reduction in the CO VMR, moving closer to the model predictions.

These variations in temperature and pressure, effectively changing the number density of the atmosphere, have a large, but expected impact on the CO VMRs. We have confidence in the ACS NIR retrievals due to their validation against MCS and ACS MIR temperature and pressure observations cite-Vandaele19,Fedorova20, as well as the consistency between CO VMR retrievals from ACS MIR and ACS NIR. We expect that further study with assimilation in the GCM, after ingesting larger and more accurate temperature and pressure data sets, will result in a closer convergence between observed and predicted CO VMR vertical profiles.

5 Comparison with ACS NIR

The NIR channel of ACS has fine enough resolution to resolve CO absorption lines among those of the CO_2 vibration-rotation band used for temperature and pressure retrievals (order 49 — 6318–6387 cm^{-1}). It was found that accounting for, and fitting the CO features improved the accuracy of temperature and pressure retrievals, and therefore those for H_2O VMR as well [4]. We have compared the preliminary ACS NIR CO VMR vertical profile retrievals, which are generally available between 25–55 km, to those from ACS MIR.

For colocated observation, both instruments are operated simultaneously during a single occultation. The vertical resolution is similar for both instruments ($\sim$ 0.5–5 km) and depends on the beta angle of the spacecraft orbit. Each observation in an occultation is not made simultaneously, the timing of both instruments is independent, and the length of time of an acquisition (which determines the vertical spacing between spectra) is unique, though similar. Therefore, each observation made by each instrument samples a slightly different airmass and tangent point location. These are similar enough that no corrections or smoothing are needed for validation.

There are three key differences between the data sets: ACS MIR has finer spectral resolution (~ 0.06 cm^{-1} compared to ~ 0.3 cm^{-1}), the ACS MIR target spectral range is free from interference from other gaseous absorptions, and the CO band observed by ACS MIR is much stronger than that observed by ACS NIR, allowing absorption features to be resolved above 100 km in altitude.

Individual VMR vertical profiles retrieved from ACS MIR and ACS NIR are shown in Supplementary Figs. 6 and 7. There is generally good agreement between the profiles, and within the estimated uncertainties. This is especially notable when there is a large difference between the predicted CO values derived from the LMD GCM (using the MY 34 dust climatology). Also shown are profiles retrieved from ACS MIR using the temperature and pressure from the GCM. Often, when there is a large difference between the ACS MIR

retrieval and the GCM, this difference is reduced when using the same temperature and pressure model as the GCM. A list of the occultations used, with time and locations information is given in Table 1.

Small scale structures on the order of magnitude of the uncertainties are not always reproduced by both data sets. Larger oscillations in the vertical profiles do appear in both data sets, implying they are likely real and due to waves or tides in the atmosphere, though this requires further study.

References

[1] Korablev, O. *et al.* The Atmospheric Chemistry Suite (ACS) of three spectrometers for the ExoMars 2016 Trace Gas Orbiter. *Space Sci. Rev.* **214**, 7 (2018).

[2] Smith, M. D. THEMIS Observations of the 2018 Mars Global Dust Storm. *J. Geophys. Res.* **124**, 2929–2944 (2019).

[3] Hase, F., Wallace, L., McLeod, S. D., Harrison, J. J. & Bernath, P. F. The ACE-FTS atlas of the infrared solar spectrum. *J. Quant. Spectrosc. Radiat. Transfer* **111**, 521–528 (2010).

[4] Fedorova, A. A. *et al.* Stormy water on Mars: The distribution and saturation of atmospheric water during the dusty season. *Science* **367**, 297–300 (2020).

[5] Olsen, K. S., Toon, G. C., Boone, C. D. & Strong, K. New temperature and pressure retrieval algorithm for high-resolution infrared solar occultation spectroscopy: analysis and validation against ACE-FTS and COSMIC. *Atmos. Meas. Tech.* **9**, 1063–1082 (2016).

[6] Vandaele, A. C. *et al.* Martian dust storm impact on atmospheric H_2O and D/H observed by ExoMars Trace Gas Orbiter. *Nature* **568**, 521–525 (2019).

[7] Fedorova, A. A. *et al.* Solar infrared occultation observations by SPICAM experiment on Mars-Express: Simultaneous measurements of the vertical distributions of H_2O, CO_2 and aerosol. *Icarus* **200**, 96–117 (2009).

[8] Maltagliati, L. *et al.* Evidence of Water Vapor in Excess of Saturation in the Atmosphere of Mars. *Science* **333**, 1868 (2011).

[9] Fedorova, A. *et al.* Water vapor in the middle atmosphere of Mars during the 2007 global dust storm. *Icarus* **300**, 440–457 (2018).

[10] Gordon, I. E. *et al.* The HITRAN2016 molecular spectroscopic database. *J. Quant. Spectrosc. Radiat. Transfer* **203**, 3–69 (2017).

[11] Sen, B., Toon, G. C., Blavier, J.-F., Fleming, E. L. & Jackman, C. H. Balloon-borne observations of midlatitude fluorine abundance. *J. Geophys. Res.* **101**, 9045–9054 (1996).

[12] Irion, F. W. *et al.* Atmospheric Trace Molecule Spectroscopy (ATMOS) Experiment Version 3 data retrievals. *Appl. Opt.* **41**, 6968–6979 (2002).

[13] Norton, R. H. & Rinsland, C. P. ATMOS data processing and science analysis methods. *Appl. Opt.* **30**, 389–400 (1991).

[14] Toon, G. C. The JPL MkIV interferometer. *Opt. Photonics News* **2**, 19–21 (1991).

[15] Wunch, D. *et al.* The Total Carbon Column Observing Network. *Phil. Trans. R. Soc. A* **369**, 2087–2112 (2011).

[16] Olsen, K. S. *et al.* Validation of the HITRAN 2016 and GEISA 2015 line lists using ACE-FTS solar occultation observations. *J. Quant. Spectrosc. Radiat. Transfer* **236**, 106590 (2019).

[17] Li, G. *et al.* Rovibrational Line Lists for Nine Isotopologues of the CO Molecule in the X $^1\Sigma^+$ Ground Electronic State. *Astrophys. J. Suppl. Ser.* **216**, 15 (2015).

[18] Gamache, R. R., Farese, M. & Renaud, C. L. A spectral line list for water isotopologues in the 1100-4100 cm^{-1} region for application to CO_2-rich planetary atmospheres. *J. Mol. Spectrosc.* **326**, 144–150 (2016).

[19] Devi, V. M. *et al.* Line parameters for CO_2- and self-broadening in the ν_3 band of HD^{16}O. *J. Quant. Spectrosc. Radiat. Transfer* **203**, 158–174 (2017).

[20] Forget, F. *et al.* Improved general circulation models of the Martian atmosphere from the surface to above 80 km. *J. Geophys. Res.* **104**, 24155–24176 (1999).

[21] Millour, E. *et al.* The Mars Climate Database (version 5.3). In *From Mars Express to ExoMars*, 68 (2018).

[22] Montabone, L. *et al.* Martian Year 34 Column Dust Climatology from Mars Climate Sounder Observations: Reconstructed Maps and Model Simulations. *J. Geophys. Res.* **125**, e06111 (2020).

Supplementary Figures

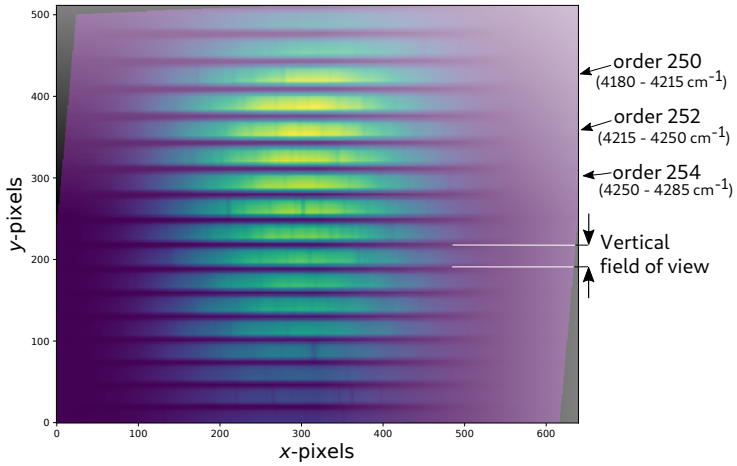

Supplementary Fig. 1: Example of a Level 1A detector frame for one observation recorded using secondary grating position 7. The colour brightness represents incident intensity (arbitrary units, brighter is more intense) and each of the visible stripes correspond to a unique diffraction order.

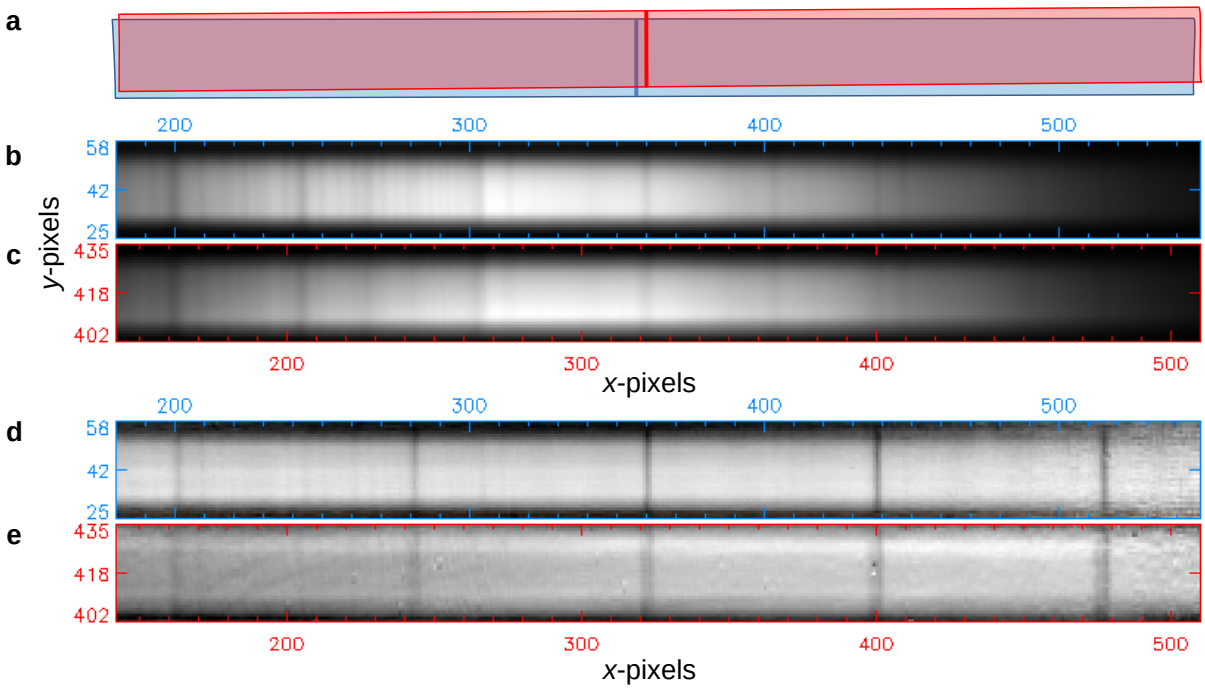

Supplementary Fig. 2: Illustration of doubled image in an ACS MIR detector frame. a) schematic representing of two offset and overlapping images, b) the lower-portion of a position 6 detector image of intensity featuring order 250, c) the upper-portion of a position 7 intensity image featuring order 250, d) the lower-portion of a position 6 transmission image with order 250, e) the upper-portion of a position 7 transmission image with order 250.

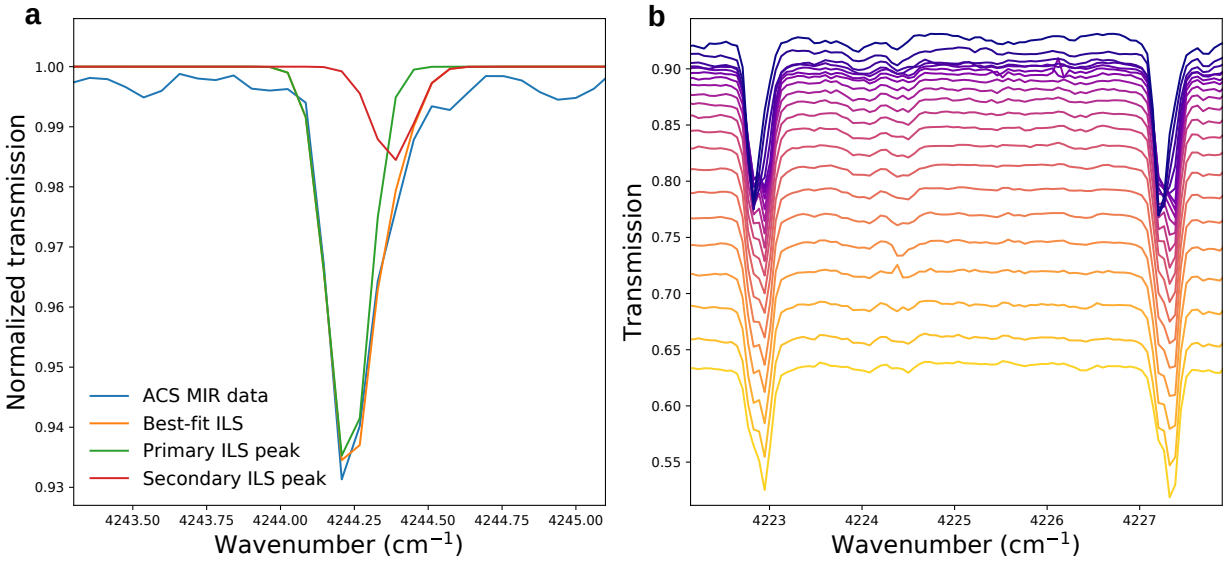

Supplementary Fig. 3: The impact of image doubling on ACS MIR spectra: a) a CO absorption feature as seen from near the slit edge, where doubling is minimized (blue), shown are contributions from a primary peak (green) and secondary peak (red) to a fitted ILS (orange); b) evolution of the doubling along detector rows for a single diffraction order, the contribution from the primary to secondary peak grows rapidly as one moves towards the detector centre from the slit edge (top of plot).

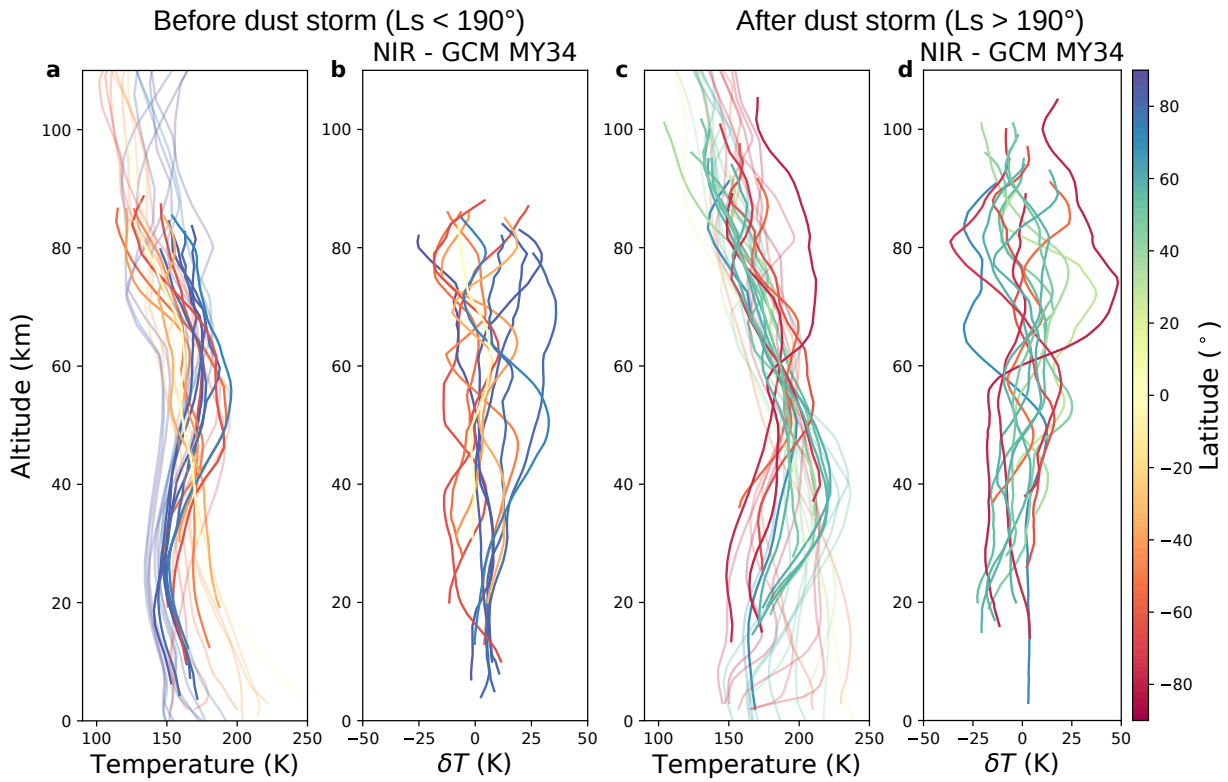

Supplementary Fig. 4: Comparison of temperature profiles (panels a) and c)) obtained from the LMD GCM using the MY 34 dust climatology (faint) and ACS NIR (solid). Colours represent latitude and the profiles are grouped by Ls to represent observations made before the onset of the global dust storm (panels a) and b)) and afterwards (panels c) and d)). Differences are shown between the NIR retrieved temperature profiles and those obtained from the GCM with MY 34 dust climatology (panels b) and d)).

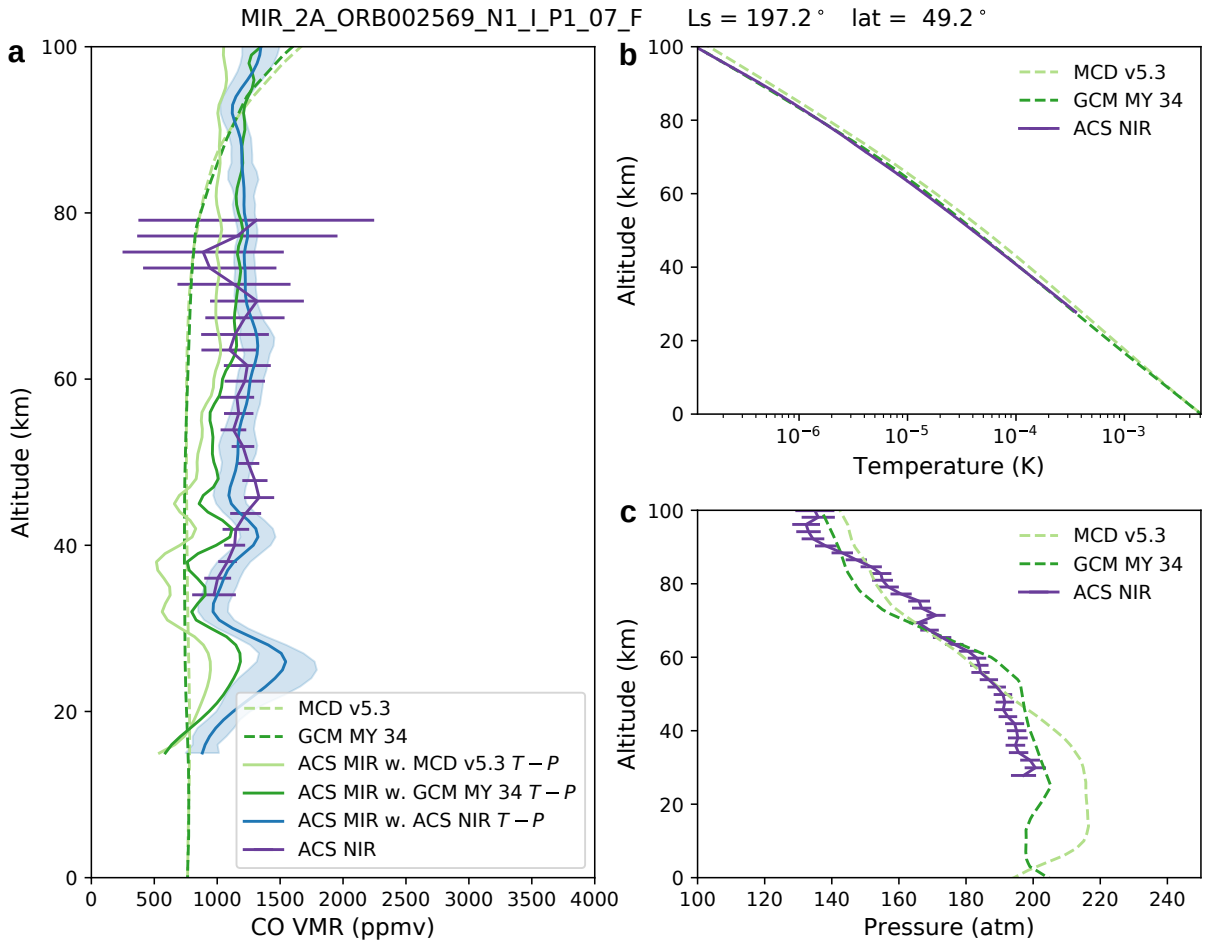

Supplementary Fig. 5: Comparison of the impact at temperature and pressure *a priori* on CO VMR retrievals: a) the CO VMR retrieved from ACS MIR data, predicted by the GCM and MCD, and retrieved from ACS NIR data; b) the pressure predicted by the GCM and MCD, and retrieved from ACS NIR data; c) the temperature predicted by the GCM and MCD, and retrieved from ACS NIR data.

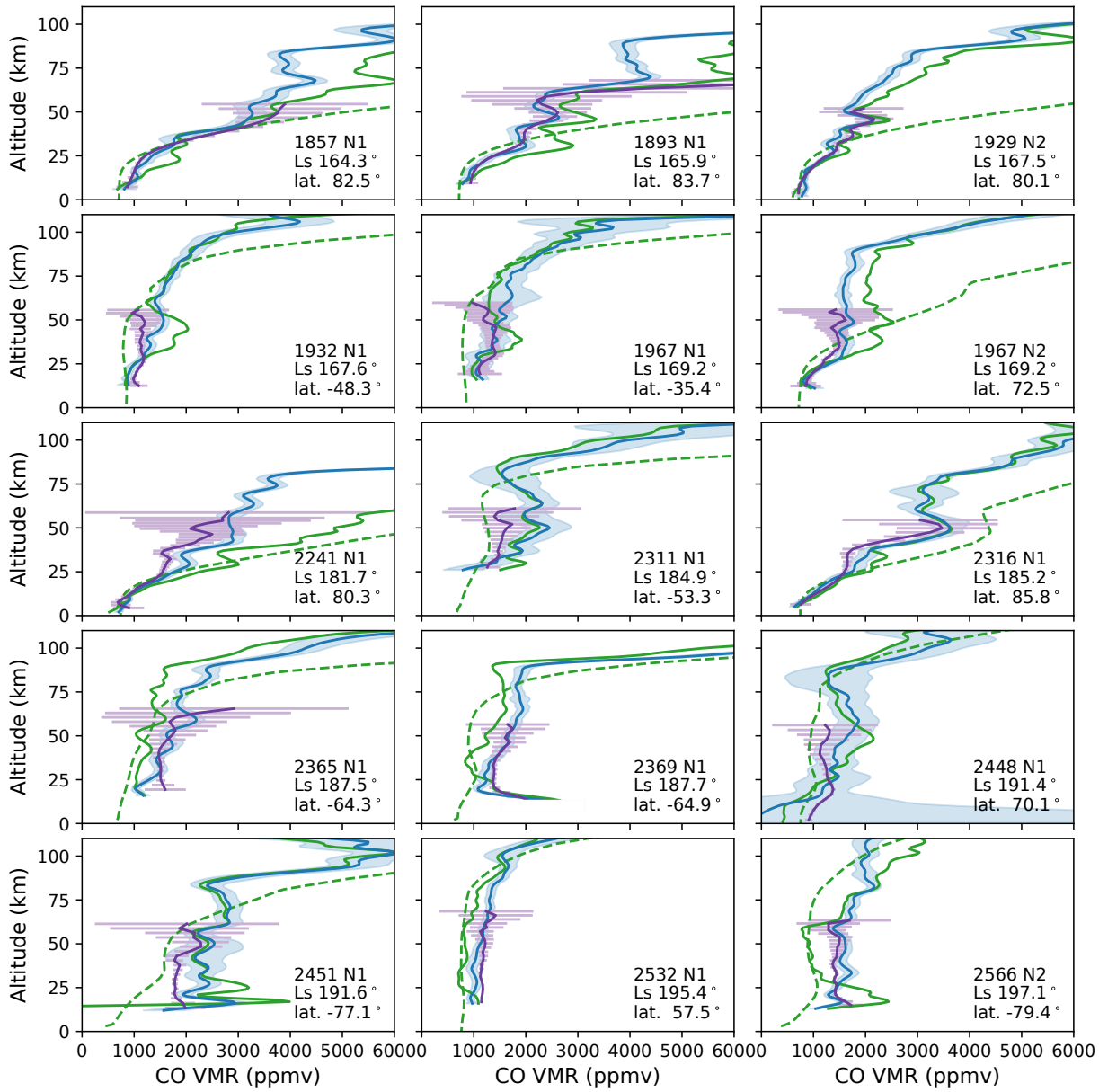

Supplementary Fig. 6: Comparison of the CO VMR retrievals from colocated ACS MIR and ACS NIR occultations. Shown are CO VMR vertical profiles obtained by running the LMD GCM using the MY 34 dust opacity climatology (dashed green), preliminary CO VMR retrievals from ACS NIR (purple), retrievals from ACS MIR using ACS NIR retrieved temperature and pressure (blue), and retrievals from ACS MIR using temperature and pressure from the GCM with MY 34 climatology (green).

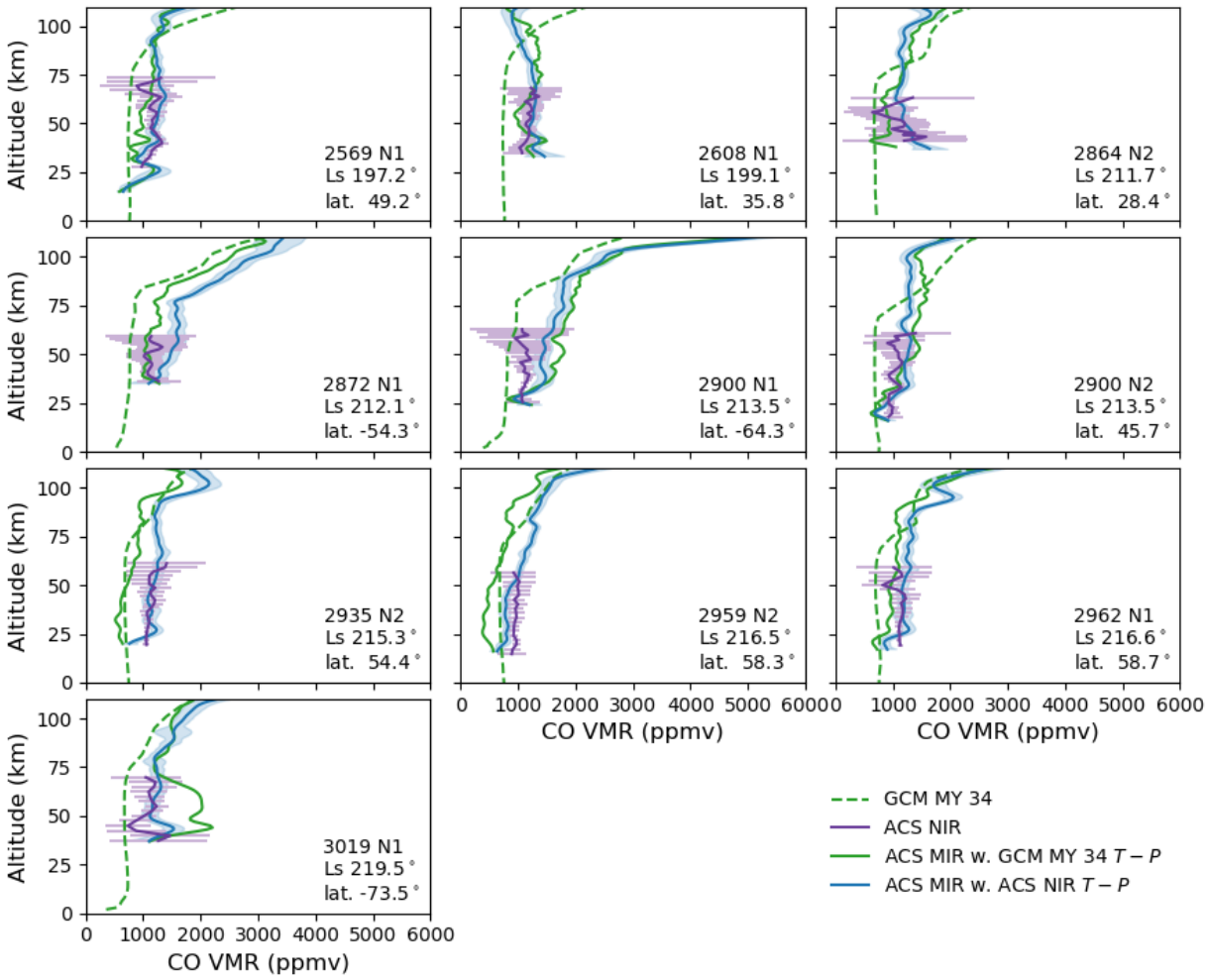

Supplementary Fig. 7: Same as Fig. 6

Table 1: Time and location information for the solar occultations used in this study.

Occultation number	Solar longitude	Latitude	Longitude	Local time
1857 N1	164.3°	82.5°	-100.8°	1.9
1893 N1	165.9°	83.7°	-101.9°	22.7
1929 N2	167.5°	80.1°	-92.7°	20.1
1932 N1	167.6°	-48.3°	152.2°	17.6
1967 N1	169.2°	-35.4°	-129.8°	17.8
1967 N2	169.2°	72.5°	-119.4°	19.0
2011 N1	171.2°	-2.7°	49.1°	18.0
2199 N1	179.7°	89.9°	114.9°	22.3
2241 N1	181.7°	80.3°	109.2°	6.3
2241 N2	181.7°	-30.4°	96.8°	6.0
2311 N1	184.9°	-53.3°	-114.3°	5.8
2316 N1	185.2°	85.8°	-97.9°	15.8
2365 N1	187.5°	-64.3°	132.9°	5.6
2369 N1	187.7°	-64.9°	17.8°	5.5
2448 N1	191.4°	70.1°	95.6°	17.1
2451 N1	191.6°	-77.1°	171.3°	4.6
2532 N1	195.4°	57.5°	-150.4°	17.3
2535 N1	195.6°	-83.3°	-158.8°	23.1
2566 N2	197.1°	-79.4°	-2.1°	20.8
2569 N1	197.2°	49.2°	-130.0°	17.4
2604 N2	198.9°	-69.9°	-31.0°	19.5
2608 N1	199.1°	35.8°	-166.5°	17.6
2645 N1	200.9°	9.6°	-144.9°	17.9
2645 N2	200.9°	-47.2°	-137.9°	18.6
2864 N2	211.7°	28.4°	-104.2°	6.5
2872 N1	212.1°	-54.3°	6.3°	4.7
2900 N1	213.5°	-64.3°	-87.1°	4.0
2900 N2	213.5°	45.7°	-50.5°	7.0
2935 N2	215.3°	54.4°	31.8°	7.4
2959 N2	216.5°	58.3°	67.7°	7.7
2962 N1	216.6°	58.7°	-17.8°	7.7
3019 N1	219.5°	-73.5°	22.9°	22.7